minerals

MDPI

Article

Stable Carbon and Oxygen Isotopic Features of Banded Travertines from the Xiagei Fissure Ridge System (Shangri-La, China)

Yaxian You [1,2], Huaguo Wen [1,2,3,4,*], Lianchao Luo [5], Zhipeng Lu [1,2] and Liang Li [6]

[1] State Key Laboratory of Oil and Gas Reservoir Geology, Chengdu University of Technology, Chengdu 610059, China
[2] Institute of Sedimentary Geology, Chengdu University of Technology, Chengdu 610059, China
[3] CNPC Key Laboratory of Carbonate Reservoir, Chengdu University of Technology, Chengdu 610059, China
[4] Key Laboratory of Deep-Time Geographical Environment Reconstruction and Application, Ministry of Natural Resources, Chengdu 610059, China
[5] Department of Earth Sciences, University of Florence, 50121 Florence, Italy
[6] College of Earth Science, Chengdu University of Technology, Chengdu 610059, China
* Correspondence: wenhuaguo08@cdut.edu.cn

Abstract: Banded travertines are important parts of fissure ridge systems, but studies on geochemical characterization of banded travertines are limited. This study investigated the lithofacies and stable carbon and oxygen isotopic features of banded travertines from Xiagei (southwestern China) to examine their formation mechanisms. Petrographic analyses of the banded travertines revealed two lithotypes: thick-laminated palisade crystalline crust and thin-laminated composite crystalline crust. $\delta^{13}C$ and $\delta^{18}O$ of the Xiagei banded travertines range from 2.82‰ to 4.50‰ V-PDB, and from −25.86‰ to −20.90‰ V-PDB. Parent CO_2 evaluation shows that the Xiagei banded travertines mainly received CO_2 from the decarbonation of marine carbonates, but the contributions of magmatic CO_2 and the dissolution of marine carbonates are also unneglectable. Significantly, the magmatic-derived CO_2 might indicate that the delamination of the lithosphere along with the asthenosphere upwelling could be taking place in the eastern Tibetan plateau. Paleotemperature calculation shows that the Xiagei travertines were precipitated from moderate- to high-temperature hot springs (44.3 to 86.8 °C). Interestingly, the thick-laminated palisade crystalline crust and thin-laminated composite crystalline crust display calculated paleotemperature between 66.6 and 86.8 °C and between 56.6 and 77.7 °C, respectively, reflecting the great role of water temperature in controlling the lithofacies of banded travertines. A comparison between the banded travertines at Xiagei and other areas also shows temperature is a non-negligible factor controlling banded travertine precipitation. However, this does not mean that water temperature is the decisive controlling factor and more studies on banded travertines are still indispensable to disclose the potential factors controlling the factors/processes affecting banded travertine lithofacies. This study provides a good example for understanding the relationship between lithofacies and stable isotopic geochemical characteristics of travertine deposits.

Keywords: banded travertine; fissure ridge; lithofacies; stable carbon and oxygen isotopes; Shangri-La

check for updates

Citation: You, Y.; Wen, H.; Luo, L.; Lu, Z.; Li, L. Stable Carbon and Oxygen Isotopic Features of Banded Travertines from the Xiagei Fissure Ridge System (Shangri-La, China). *Minerals* **2023**, *13*, 76. https://doi.org/10.3390/min13010076

Academic Editors: Francesca Giustini and Mauro Brilli

Received: 19 November 2022
Revised: 27 December 2022
Accepted: 28 December 2022
Published: 3 January 2023

Copyright: © 2023 by the authors. Licensee MDPI, Basel, Switzerland. This article is an open access article distributed under the terms and conditions of the Creative Commons Attribution (CC BY) license (https://creativecommons.org/licenses/by/4.0/).

1. Introduction

Fissure ridges are common elongated travertine build-ups with open or (partly) sealed central fissures and inclined flanks dipping away from the central fissures in geothermal areas [1–10]. Travertine fissure ridges are closely related with tectonic activity, such as faulting and earthquakes [2–7,10–16]; and, as one of carbonate sediments, their geochemistry bears abundant tectonic-environment information [17]. Travertine deposits in fissure ridge systems can be divided into two types: bedded travertines and banded travertines (also named banded veins, carbonate/calcite veins, etc.) [3–6,11,16]. The former are epigean/surface carbonate deposits after the emergence of thermal water from orifices/vents and are deposits

dipping gently away from nearly vertical, irregular central fissures, while the latter are less porous hypogean/underground subvertical to vertical carbonate deposits (i.e., formed during the upwelling of thermal fluid along the conduit) and are often small in scale (commonly millimeter-scale to decimeter-scale in width although meter-scale or even more large banded travertines were also reported) [1,4–6,11,12,18–20].

Previous studies on banded travertines in fissure ridge systems mainly focus on their distribution, geometry, mineralogy, texture, and tectonic implications [1,3,4,6,9,11,12,15,16,20–22]. There were also some studies on the geochemical and lithofacies characteristics of banded travertines [18,23–26], but rare studies focused on the relationship between geochemical signatures and lithofacies of banded travertines. Theoretically, the chemical composition of fluids in hypogean conduits might change during the formation of banded travertines and such variation might change both the geochemical signatures and lithofacies of banded travertines.

In this study, careful lithofacies and stable carbon and oxygen isotope analyses of banded travertines at Xiagei were performed to determine their genesis and the relationship between their lithofacies and stable isotope carbon and oxygen isotope compositions. Hydrochemical analyses of modern hot springs at Xiagei and mineralogical and petrological investigations of the Xiagei travertines were also conducted to aid in the interpretation of the Xiagei banded travertines. The findings may help us better understand the formation mechanism of banded travertines.

2. Geological Background

The Shangri-La area, Yunnan Province, China is located near the Jinshajiang fault zone, one of the most active tectonic zones in the Tibetan plateau (Figure 1A). Deposits exposed near the Shangri-La city are mainly composed of Pleistocene to Holocene lacustrine and alluvial-pluvial sediments (e.g., sandy conglomerate, gravel and clay) and Late Triassic sedimentary rocks (including both siliciclastic and carbonate rocks), but Late Paleozoic carbonate rocks and Triassic intrusive igneous rocks are also partly exposed in Shangri-La (Figure 1B) [27–32]. This area was continuously impacted by the subduction of the Paleo- and Meso-Tethyan oceans and continental collisions following their closures during the Mesozoic and the India-Asian collision during the Cenozoic [33–35]. There are lots of N-S trending faults and associated secondary faults [30]. These large-scale faults and fractures provided favorable conduits for the circulation and upwelling of geothermal fluids in Shangri-La and generated a large number of hot springs and associated spring deposits [29–31]. Five key fault zones controlling the hydrothermal activities have been reported in the Shangri La area: N-W striking Zhongdian reverse fault zone (F1), NWW-SEE-striking Yanggu fault zone (F2), N-S striking Gezanhe-Are reverse fault zone (F3), N-NE-striking Kangshi normal fault zone (F4), near E-W trending Tianshengqiao reverse fault zone (F5) (Figure 1B) [30].

The Xiagei area (99°51′20″ E, 27°47′00″ N), is situated to the northeast of the Shangri-La city and lies on the Tianshengqiao fault zone (Figure 1B). Some NW-SE trending and NE-SW trending travertine fissure ridges were developed at Xiagei (Figure 2A,B) and ranged from 25 to 140 m long and up to 120 m wide. The longest fissure ridge at Xiagei (i.e., Fr1 in Figure 2) is a NW-SE trending system and laterally extends around 140 m long (Figure 2A–C). In addition to travertine fissure ridges, some meter-scale travertine mounds/cones, waterfalls, and terraced slopes were also observed near the fissure ridges. Furthermore, a few hot springs occurred in the Xiagei fissure ridge system although their volumetric flow rates were often very low. Active hot springs at Xiagei discharged mid-temperature (41.4 to 63.1 °C) HCO_3-Ca and HCO_3-Ca-Na type waters with slightly acidic to near neutral pH (5.57 to 7.67) and high TDS (1249 to 1468 mg/L) [32]. Isotopic values of the Xiagei hot spring waters were reported to be between −15‰ and −16.2‰ V-SMOW for $\delta^{18}O_{water}$ and between −128.3‰ and −133.4‰ V-SMOW for δD_{water}, which are close to the meteoric water line and are indicative of a meteoric origin [32].

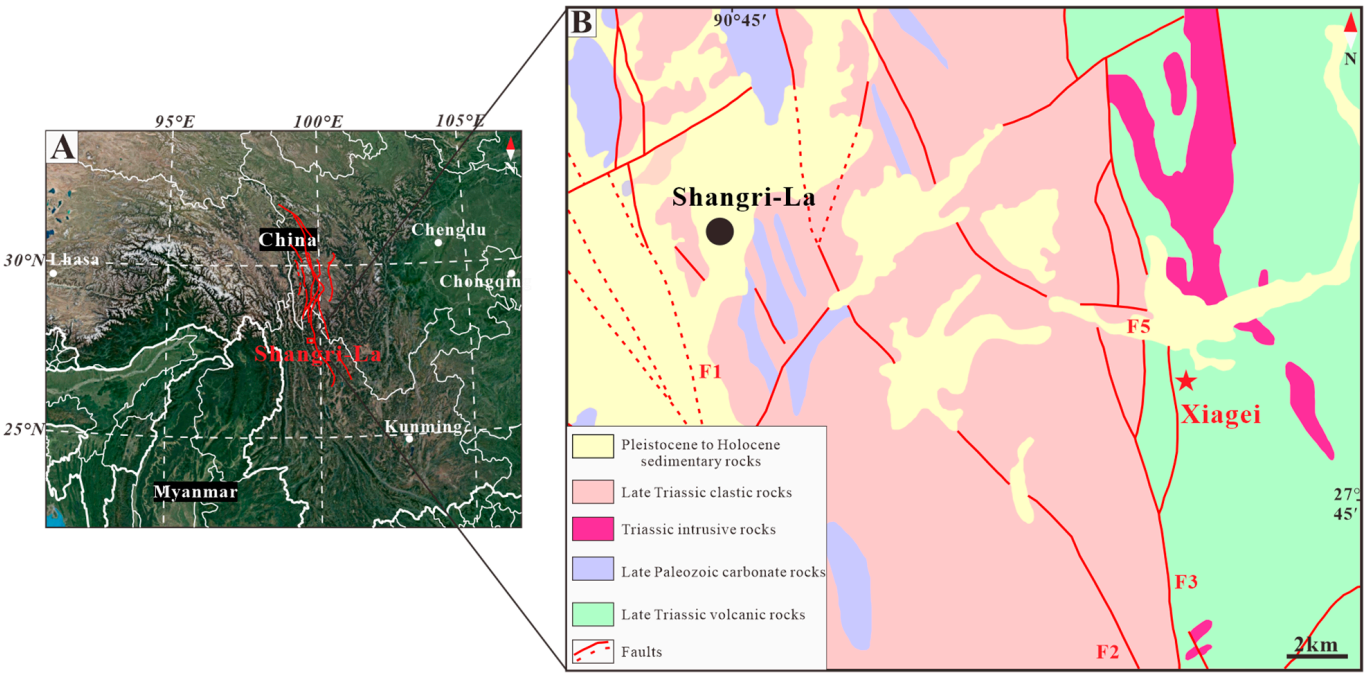


Figure 1. (**A**) Location of the Shangri-La area, northwest of Yunnan Province (China); Red lines: Jinshajiang fault zone. (**B**) Geologic map of Xiagei and surrounding region (modified from Zheng [32]). F2: NWW-SEE-striking Yanggu fault zone, F3: N-S striking Gezanhe-Are reverse fault zone, F5: near E-W trending Tianshengqiao reverse fault zone.

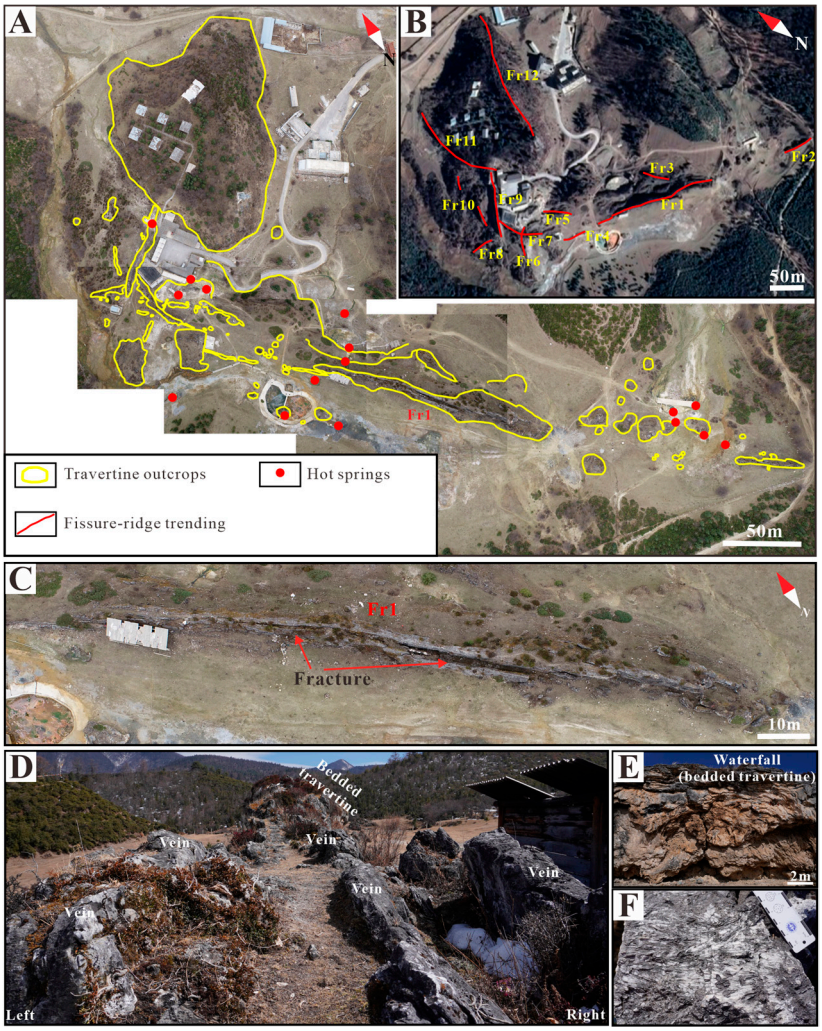


Figure 2. Photographs illustrating the travertine deposits at Xiagei. (**A**) UAV images splicing, indicating the travertine deposit outcrops and the distribution of hot springs. (**B**) An aerial photograph from Google Maps, highlighting the main fissure ridges. (**C**) Images of the studied fissure ridge travertines. (**D**) A general view of the fissure-ridge-type travertines at Xiagei with banded and bedded travertines. (**E**) Examples of travertine waterfalls with thick-bedded travertines. (**F**) Details of thick-laminated palisade crystalline crust.

3. Methods

Banded travertine samples were collected from the top area of Fr1 fissure ridge at Xiagei, where banded travertines were well exposed (Figure 2D). Some fossil bedded travertine samples and modern travertine samples were also collected at Xiagei. To analyze their petrological, mineralogical, and textural characteristics, nineteen thin sections were made from eighteen fossil travertine samples and were examined under an Eclipse LV100POL optical polarizing microscope (Nikon, Tokyo, Japan) at Chengdu University of Technology.

Stable carbon and oxygen isotope analyses were performed on 80 banded travertine samples, 12 bedded travertine samples, and three modern travertine samples at Yangtze University. Samples for $\delta^{13}C$ and $\delta^{18}O$ analyses were first dried and ground into powder. A Delta V Advantage isotope ratio mass spectrometer (Thermo Fisher Scientific, Waltham, MA, USA) was employed to measure the $\delta^{13}C$ and $\delta^{18}O$ values and the final results were calibrated to V-PDB (Vienna Pee Dee Belemnite) scale. Analytical errors of $\delta^{13}C$ and $\delta^{18}O$ are $\leq$0.2‰ and $\leq$0.3‰, respectively.

Water samples of three hot springs were also collected and analyzed to aid in the interpretation of banded travertines. Main physicochemical parameters of the water samples,

including water temperature (T_{water}), pH, and total dissolved solids (TDS), were measured in the field using a portable water quality meter (Eutech CyberScan COND 610 meter, Eutech Instruments, San Francisco, CA, USA) and a portable pH meter (Lichen, Shanghai, China). Water samples for lab analyses were filtered using a 0.45 μm filtration membrane and were stored in 50 ml polyethylene plastic bottles. Concentrations of CO_3^{2-} and HCO_3^- of water samples were determined by titration [36] soon after the sampling. Concentrations of other anions (F^-, Br^-, Cl^- and SO_4^{2-}) and common cations (Na^+, K^+, Ca^{2+} and Mg^{2+}), and dissolved SiO_2 were measured with an ion chromatography system (Dionex ICS-1100, Thermo Fisher Scientific, Waltham, MA, USA; 883 Basic IC plus, Metrohm, Herisau, Switzerland) at Analytical Laboratory of Beijing Research Institute of Uranium Geology (China). PHREEQC (ver. 3) with the WATEQ4F database [37] was utilized to calculate the saturation index of calcite ($SI_{calcite}$) and partial pressure of (dissolved) CO_2 ($\log P_{CO_2}$). Stable hydrogen (δD_{water}) and oxygen ($\delta^{18}O_{water}$) isotopes of the three collected water samples were also measured using an isotope ratio mass spectrometer (Delta V Advantage, Thermo Fisher Scientific, Waltham, MA, USA) at Analytical Laboratory of Beijing Research Institute of Uranium Geology (China). $\delta^{18}O_{water}$ and δD_{water} values were calibrated based on the Vienna Standard Mean Ocean Water(V-SMOW) scale.

4. Results

4.1. Fissure Ridge Travertines at Xiagei

The Xiagei hydrothermal system is characterized by the occurrence of multiple active springs and widespread (modern and fossil) travertines (Figure 2). Travertines cropping out in the study area are ca. 0.08 km^2 and contain twelve fissure ridges. The spatial distribution of the Xiagei fissure ridges is mapped in Figure 2A,B. It is striking that the Xiagei fissure ridges developed with two entirely different trends (NE-trending and NW-trending) and displayed varying lengths (25 to 140 m) and widths (1 to 120 m). Interestingly, some NE-trending fissure ridges were found to cut through some NW-trending fissure ridges, implying that there were at least two periods of fault activity at Xiagei.

A common characteristic of the Xiagei fissure ridges is that their central fissures are more or less filled with banded travertines. However, not all the banded travertines were well exposed and easily accessible, and only the longest fissure ridge (i.e., Fr1 in Figure 2A–C) cropped out thick and relatively complete banded travertines. Fr1 fissure ridge is a NW-trending system with a length of around 140 m, a maximum width of near 20 m, and a maximum height of about 20 m (Figure 2A–C). Several small travertine mounds and a 35-meter-long fissure ridge developed to the northwestern of the Fr1 fissure ridge and exhibited the same trend to the Fr1 fissure ridge (Figure 2A). The central fissure of Fr1 fissure ridge was not fully sealed by banded travertines. Soils, vegetation, and open fissures were also observed within the central fissure of Fr1 (Figure 2C).

4.2. Spring Water

Chemical composition and $\delta^{18}O_{water}$ and δD_{water} of hot spring waters at Xiagei were reported in Table 1. The results show that the studied hot springs are characterized by slightly acidic to near neutral pH values and water temperatures between 31.7 °C and 58 °C. HCO_3^- (953 to 998 mg/L), Na^+ (231 to 249 mg/L), and Ca^{2+} (120 to 151 mg/L) are the main components of the spring waters, while some SO_4^{2-} (36.9 to 133 mg/L), Cl^- (26.5 to 31.3 mg/L), K^+ (16.4 to 20.5 mg/L), SiO_2 (20.4 to 83.2 mg/L), and minor F^- (2.95 to 9.84 mg/L) and Mg^{2+} (8.82 to 9.89 mg/L) are also present. $\delta^{18}O_{water}$ and δD_{water} values of the three studied springs are between −15.3‰ and −14.5‰ V-SMOW (average = −14.9‰ V-SMOW), and between −133.9‰ and −128.7‰ (average = −133.3‰ V-SMOW), respectively (Table 1). The here obtained ion concentrations, $\delta^{18}O_{water}$, and δD_{water} are very close to the data reported earlier by Zheng [32]. Calculated $SI_{calcite}$ and $\log P_{CO_2}$ in hot spring waters from Xiagei range from 0.14 to 0.69 and from −0.54 to −0.96, respectively (Table 1).

Table 1. Water chemistry, δ^2H_{water} and $\delta^{18}O_{water}$ values of hot springs at Xiagei.

Location	T (°C)	pH_{field}	Alkalinity (mg/L)	HCO_3^- (mg/L)	F^- (mg/L)	Cl^- (mg/L)	SO_4^{2-} (mg/L)	Na^+ (mg/L)	K^+ (mg/L)	Mg^{2+} (mg/L)	Ca^{2+} (mg/L)	SiO_2 (mg/L)	δ^2H_{water} (‰, V−SMOW)	$\delta^{18}O_{water}$ (‰, V−SMOW)	SI_C	log pCO_2
S1	32	6.98	842	998	3.0	27.5	65.1	231	16.4	8.8	148	20.4	−133.9	−14.9	0.64	−0.96
S2	58	6.81	825	993	3.2	31.3	36.9	249	20.5	9.9	120	25.4	−137.3	−15.3	0.69	−0.61
S3	31.7	6.52		953	9.8	26.5	133	234	17.3	9.6	151	83.2	−128.7	−14.5	0.14	−0.54
YX2-1 [a]	63	6.70	762	928.7	5.9	24.5	33	250	14.9	29.2	65.9	85.4	−130	−16.2	0.36	−0.49
YX2-3 [a]	50.5	5.57	649	790.8	5.3	21.3	29.8	219	27.6	25.5	60.1	68.2	−130.2	−15.1	−1	0.48
YX2-5 [a]	41.4	7.66	622	759.1	5.8	26.1	35.1	255	29.9	16.9	35.9	80.8	−128.3	−15	0.72	−1.7
YX2-6 [a]	47.3	7.67	745	908	4.3	26.6	35.7	234	19.7	15.6	89.8	85.4	−131.5	−15.2	1.25	−1.6
YX2-7 [a]	63.1	7.56	781	951.9	5.9	26.1	35.1	251	15	34.0	63.9	83.1	−133.4	−15.6	1.18	−1.35

(blank = no specific data); [a] reference from Zheng [32].

4.3. Lithofacies of Banded Travertines

According to the travertine lithofacies classification of Gandin and Capezzuoli [38], the Xiagei banded travertines belong to abiotic crystalline crust. The Xiagei banded travertines is characteristic by striking lamination, but laminae of the Xiagei banded travertines show varying thickness from tens of micrometers to several centimeters. Additionally, the main components of the Xiagei banded travertines are diverse and include dendritic crystals, fan crystals, platy crystals, banded palisade crystals and granular crystals. Thus, the Xiagei banded travertines were here further divided into thick-laminated palisade crystalline crust and thin-laminated composite crystalline crust.

The thick-laminated palisade crystalline crust is not very common in the Xiagei banded travertines and stands out by the alternation of thick layers over one centimeter in thickness (Figure 3). Each thick layer is composed of abundant large palisade crystals often ranging from 1 to 3 cm long and over 0.4 mm wide and may contain several growth lines (Figure 3A,C). The growth lines were visible in both hand specimens and thin sections, but they were not laterally continuous. Palisade crystal growth was not terminated at most of the growth lines (e.g., Figure 3A).

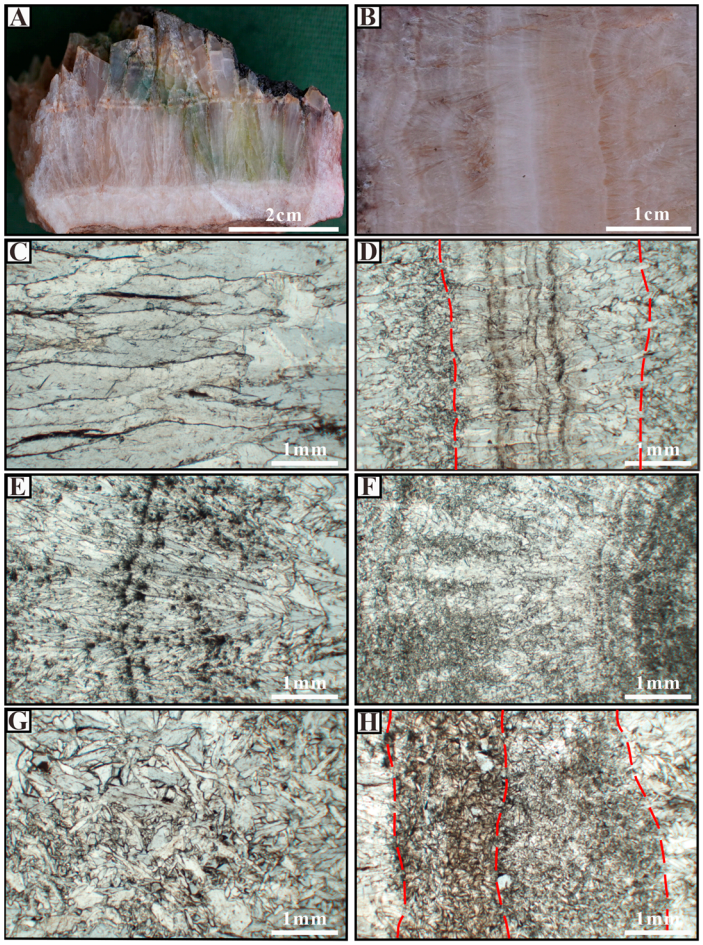


Figure 3. Hand specimens (**A**,**B**) and microphotographs (**C**–**H**) of the main petrographic characteristics of the studied banded travertines. (**A**) Cross-section of thick-laminated palisade crystalline crust. (**B**) Polished side of thin-laminated composite crystalline crust. (**C**) cm-size elongated palisade crystals. (**D**) Short-columinar calcite crystals. (**E**) Feather-like dendritic crystals. (**F**) Dendritic crystals with blurry edges and numerous microcrystals filling intercrystalline pores. (**G**) Willow leaf bladed-like calcite crystals, and intercrystalline microcrystals. (**H**) Bands of dark granular crystals and calcite micrite.

Compared with the thick-laminated crystalline crust, the thin-laminated composite crystalline crust is characterized by the alternation of thin layers (less than 1 cm in thickness). Composition of the thin layers is very complex. Short-columnar crystals, dendritic crystals, platy crystals, fan crystals, granular crystals and calcite micrite were all found as possible main components of the thin layers. In many cases, the thin layers in the thick-laminated crystalline crust only consist of one component, such as the short palisade crystal layer in Figure 3D and the dendritic crystal layer in Figure 3E. However, in some cases, thin layers of the thick-laminated crystalline crust may contain several different components, such as the co-occurrence of dendritic crystals and micrite in Figure 3F.

Short-columnar crystals are the most common components in the thin-laminated composite crystalline crust from Xiagei and is dominantly composed of columnar-like calcite crystal often ranging from 3 to 8 mm in length, significantly shorter than the palisade crystals forming the thick-laminated palisade crystalline crust. Calcite micrite was observed among the short-palisade crystals but was not common in all samples. Dendrite crystals were found in many samples and were characterized by elongated trunks with plentiful branches. In terms of crystal morphologies, the dendrite crystals from Xiagei can be divided into two types: dendritic crystals (3 to 5 mm in length) coexist with micrites (Figure 3F) and typical feather-like calcite crystals (up to 4mm in length; Figure 3E). Platy crystals (Figure 3G) were present in some calcite veins at Xiagei and consisted of willow leaf bladed-like calcite with lengths commonly lower than 1 mm and thicknesses below 0.3 mm. The platy crystals co-appeared with some micrite (Figure 3G) and/or fan crystals. A few samples from the thin-laminated composite crystalline crust contained fan crystals and granular crystals. The fan crystals generally have high length-width ratio (≈1.5) and have varying sizes (up to 3.5 mm long and 2 mm wide). Granular crystals (Figure 3H) here refer to subhedral to anhedral calcite crystals. The granular crystals in the Xiagei thin-laminated composite crystalline crust display varying sizes from 0.15 mm to tens of microns in diameter.

4.4. Stable Isotopes

Stable oxygen and carbon isotope compositions of the Xiagei travertines were listed in Table 2 and illustrated in Figures 4 and 5. The studied banded travertines show narrow variations of $\delta^{13}C$ from 2.82‰ to 4.50‰ V-PDB (average = 3.52‰ V-PDB) and $\delta^{18}O$ from −25.86‰ to −20.90‰ V-PDB (average = −23.66‰ V-PDB). The thick-laminated palisade banded travertines display different $\delta^{13}C$ and $\delta^{18}O$ ranges from the thin-laminated composite banded travertines. The former show $\delta^{13}C$ between 2.82‰ and 3.74‰ V-PDB and $\delta^{18}O$ between −25.86‰ and −22.64‰ V-PDB, while the later display more positive $\delta^{13}C$ (3.37‰ and 4.50‰ V-PDB) and $\delta^{18}O$ (−24.45‰ and −20.90‰ V-PDB). A good positive correlation (R^2 = 0.8, n= 80) was also found between $\delta^{13}C$ and $\delta^{18}O$ of the banded travertines.

Table 2. $\delta^{13}C$, $\delta^{18}O$, calculated paleo-temperature (T_{cal}), $\delta^{13}C_{parent\ CO_2}$ of the Xiagei fossil and recently formed travertines. The depositional paleo-temperature (°C) of the travertines was calculated following the equation from Kele et al. [39] and using $\delta^{18}O_{water}$ = −15.2‰; the $\delta^{13}C_{parent\ CO_2}$ was calculated following the equation from Chacko et al. [40] and using the calculated paleo-temperatures.

Sample ID	Travertine Classification	$\delta^{13}C$ (‰, V-PDB)	$\delta^{18}O$ (‰, V-PDB)	$\delta^{18}O$ (‰, V-SMOW)	T_{cal} (°C)	$\delta^{13}C_{parent\text{-}CO_2}$ (‰, V-PDB)
1	TP	3.63	−22.98	7.23	68.6	−2.68
2		3.74	−22.97	7.24	68.6	−2.57
3		3.56	−22.64	7.58	66.6	−2.93
4		3.03	−23.82	6.37	73.7	−2.85
5		3.14	−24.15	6.02	75.8	−2.55
6		3.15	−23.93	6.25	74.4	−2.67

Table 2. *Cont.*

Sample ID	Travertine Classification	$\delta^{13}C$ (‰, V-PDB)	$\delta^{18}O$ (‰, V-PDB)	$\delta^{18}O$ (‰, V-SMOW)	T_{cal} (°C)	$\delta^{13}C_{parent\text{-}CO_2}$ (‰, V-PDB)
7		3.05	−25.52	4.61	84.5	−1.96
8		2.94	−25.68	4.45	85.5	−1.98
9		2.93	−25.72	4.4	85.9	−1.98
10		3.10	−25.21	4.93	82.5	−2.07
11		3.09	−25.68	4.45	85.5	−1.83
12		3.29	−25.41	4.73	83.7	−1.77
13		3.01	−24.98	5.17	81	−2.27
14		2.97	−25.37	4.77	83.5	−2.11
15		3.08	−25.58	4.55	84.9	−1.89
16		2.90	−25.40	4.73	83.7	−2.16
17		3.01	−25.55	4.58	84.7	−1.98
18		3.00	−25.86	4.26	86.8	−1.83
19		3.21	−25.47	4.66	84.2	−1.82
20		3.09	−25.61	4.52	85.1	−1.86
21		3.22	−25.39	4.74	83.7	−1.84
22		2.83	−25.46	4.67	84.1	−2.21
23		2.82	−25.51	4.62	84.4	−2.19
24		3.10	−25.21	4.93	82.5	−2.07
25		2.91	−25.63	4.5	85.2	−2.04
26		3.54	−22.95	7.26	68.4	−2.78
27		3.54	−23.01	7.2	68.8	−2.76
28		3.37	−23.98	6.2	74.7	−2.42
29		3.80	−23.21	6.99	70	−2.38
30		3.63	−23.48	6.71	71.7	−2.42
31		3.62	−23.27	6.93	70.4	−2.53
32		3.60	−23.16	7.04	69.7	−2.62
33		3.88	−22.86	7.35	67.9	−2.50
34		3.54	−23.26	6.94	70.3	−2.63
35		3.66	−23.76	6.43	73.3	−2.25
36	TC	3.74	−23.82	6.37	73.7	−2.13
37		3.49	−23.39	6.81	71.1	−2.61
38		3.58	−23.59	6.6	72.3	−2.42
39		3.81	−23.13	7.08	69.5	−2.43
40		3.93	−22.78	7.44	67.4	−2.48
41		3.43	−24.02	6.16	74.9	−2.34
42		3.48	−23.93	6.25	74.4	−2.34
43		3.70	−23.41	6.78	71.3	−2.38
44		3.70	−23.81	6.37	73.7	−2.17
45		3.57	−23.48	6.71	71.7	−2.48
46		3.40	−23.62	6.57	72.5	−2.57

Table 2. *Cont.*

Sample ID	Travertine Classification	$\delta^{13}C$ (‰, V-PDB)	$\delta^{18}O$ (‰, V-PDB)	$\delta^{18}O$ (‰, V-SMOW)	T_{cal} (°C)	$\delta^{13}C_{parent\text{-}CO_2}$ (‰, V-PDB)
47		4.19	−21.50	8.75	60	−2.90
48		3.73	−22.29	7.94	64.5	−2.95
49		3.49	−22.78	7.44	67.4	−2.92
50		3.60	−23.00	7.21	68.7	−2.71
51		3.54	−23.39	6.81	71.1	−2.56
52		3.85	−22.80	7.41	67.6	−2.55
53		4.11	−22.03	8.21	63	−2.70
54		3.45	−23.27	6.93	70.4	−2.70
55		3.41	−23.48	6.72	71.6	−2.64
56		3.69	−23.65	6.54	72.6	−2.29
57		3.66	−23.45	6.74	71.5	−2.41
58		3.67	−23.34	6.86	70.8	−2.44
59		3.67	−23.53	6.67	71.9	−2.36
60		3.80	−23.13	7.08	69.5	−2.44
61		4.04	−22.74	7.47	67.2	−2.39
62		3.51	−23.19	7.01	69.9	−2.70
63		3.80	−22.98	7.23	68.6	−2.51
64		3.84	−22.98	7.23	68.6	−2.47
65		3.69	−23.21	6.99	70	−2.50
66		3.56	−23.39	6.8	71.1	−2.54
67		3.48	−23.16	7.04	69.7	−2.74
68		3.69	−23.18	7.02	69.8	−2.51
69		3.85	−22.12	8.12	63.6	−2.91
70		3.64	−22.62	7.6	66.5	−2.86
71		3.76	−23.00	7.21	68.7	−2.55
72		3.53	−23.04	7.16	69	−2.74
73		3.75	−22.61	7.62	66.4	−2.75
74		3.88	−21.95	8.29	62.6	−2.97
75		4.24	−21.46	8.8	59.7	−2.88
76		3.80	−22.68	7.54	66.8	−2.67
77		3.73	−22.72	7.5	67	−2.72
78		3.75	−20.90	9.38	56.6	−3.65
79		4.50	−22.39	7.84	65.1	−2.13
80		3.66	−24.45	5.71	77.7	−1.88

Table 2. *Cont.*

Sample ID	Travertine Classification	$\delta^{13}C$ (‰, V-PDB)	$\delta^{18}O$ (‰, V-PDB)	$\delta^{18}O$ (‰, V-SMOW)	T_{cal} (°C)	$\delta^{13}C_{parent\text{-}CO_2}$ (‰, V-PDB)
81	BT	4.49	−21.79	8.45	61.7	−2.45
82		4.49	−21.96	8.29	62.6	−2.36
83		4.71	−20.90	9.37	56.7	−2.69
84		4.84	−20.97	9.3	57	−2.52
85		5.16	−20.23	10.06	53	−2.59
86		4.88	−20.93	9.34	56.8	−2.52
87		4.68	−21.29	8.98	58.7	−2.53
88		4.98	−20.91	9.36	56.7	−2.42
89		5.31	−20.68	9.6	55.4	−2.20
90		4.40	−22.00	8.24	62.9	−2.43
91		4.38	−21.91	8.33	62.4	−2.49
92		5.51	−20.41	9.88	53.9	−2.16
93	RFT	5.98	−21.28	8.98	58.7	−1.24
94		5.66	−21.86	8.39	62	−1.25
95		6.81	−18.58	11.76	44.3	−1.80

TP = thick-laminated crystalline crust; TC = thin-laminated composite crystalline crust; BT = bedded travertines; RFT = recently formed travertines.

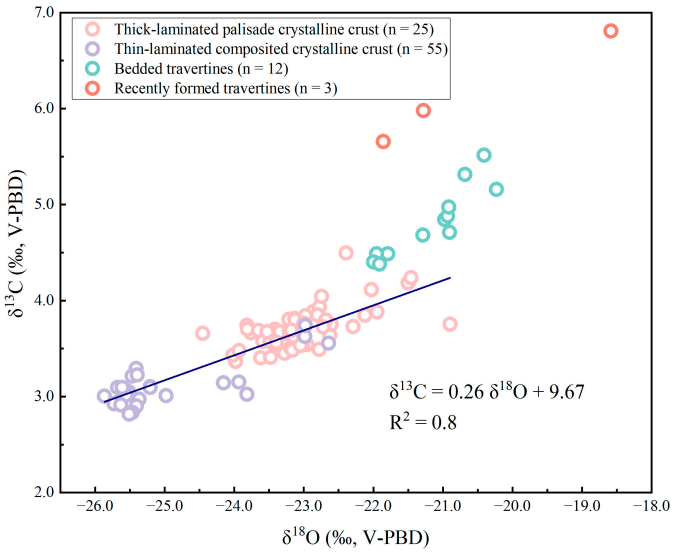


Figure 4. $\delta^{13}C$ and $\delta^{18}O$ of thick-laminated palisade crystalline crust, thin-laminated composite crystalline crust, bedded travertines and recently formed travertines at Xiagei. n = the number of samples.

Bedded travertines from Xiagei show narrower $\delta^{13}C$ and $\delta^{18}O$ ranges compared to the fossil banded travertines (Table 2, Figure 5). They have $\delta^{13}C$ values from 4.40‰ to 5.51‰ V-PDB (average = 4.82‰ V-PDB) and $\delta^{18}O$ values from −22.00‰ to −20.23‰ V-PDB (average = −21.17‰ V-PDB). $\delta^{13}C$ values of recently formed travertines from Xiagei are from 5.66‰ to 6.81‰ V-PDB (average = 6.15‰ V-PDB), slightly higher that $\delta^{13}C$ of the banded travertines. Comparatively, $\delta^{13}O$ of the recently formed travertines from Xiagei is more negative than that of the banded travertines and varies from −21.86‰ to −18.58‰ V-PDB (average = −20.57‰ V-PDB).

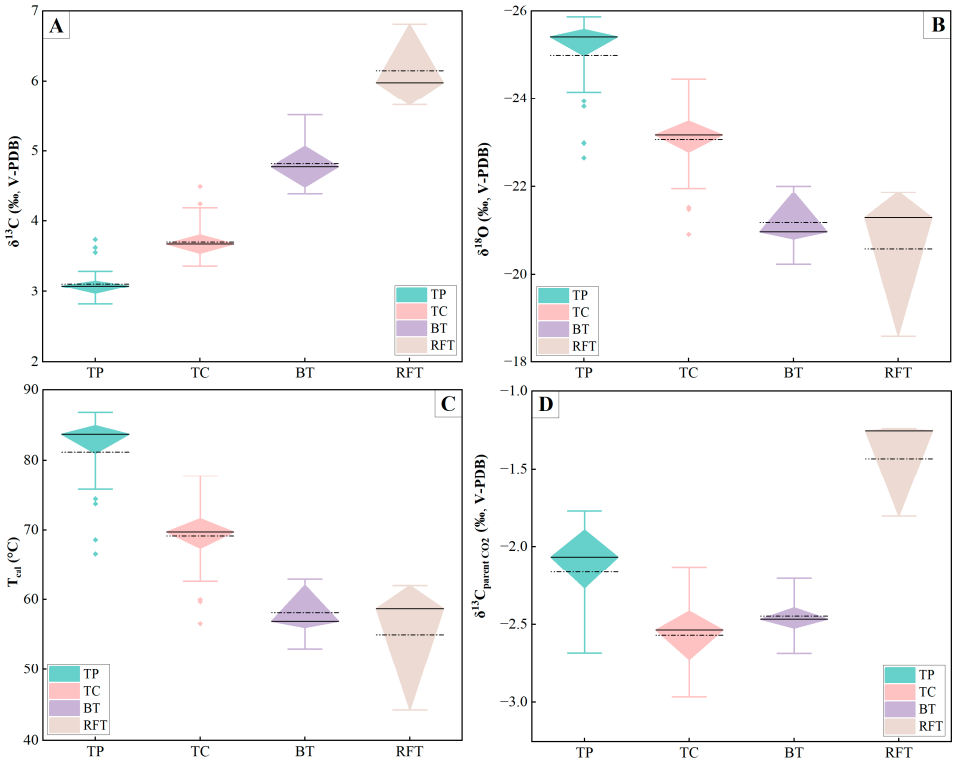


Figure 5. Diamond box plots showing the relationships between lithotypes and $\delta^{13}C$ (**A**), between lithotypes and $\delta^{18}O$ (**B**), between lithotypes and T_{cal} (**C**), and between lithotypes and $\delta^{13}C_{parent\ CO_2}$ (**D**). thick-laminated crystalline crust (TP), thin-laminated composite crystalline crust (TC), bedded travertines (BT) and recently formed travertines (RFT). Horizontal dark lines referred to the median values, while dot-dash lines referred to the mean values.

5. Interpretation and Discussion

5.1. Paleo-Temperatures for Banded Calcite Precipitation

Paleotemperature evaluation is of great importance in studies on fossil travertine systems because it can disclose the depositional conditions of travertines. The $CaCO_3$-H_2O oxygen isotopic geothermometer is considered to be a powerful tool for assessing the temperature of carbonate precipitation since the oxygen isotope fractionation will take place between the calcite/aragonite and water during naturally precipitated carbonates [5,6,39,41–43]. The calcite–water oxygen isotope fractionation equation developed by Kele et al. [39] (i.e., Equation (1)) is commonly utilized to predict the water temperature of fossil travertines because this equation decreases the influences of degassing and evaporation on the calculated results:

$$1000\ \ln\alpha_{(travertine\text{-}water)} = 20{,}000/T_{cal} - 36 \quad (1)$$

where T_{cal} = calculated paleotemperature in Kelvin and $\alpha_{(travertine\text{-}water)}$ is expressed as:

$$\alpha_{(travertine\text{-}water)} = (\delta^{18}O_{travertine} + 1)/(\delta^{18}O_{water} + 1) \quad (2)$$

where $\delta^{18}O_{travertine}$ and $\delta^{18}O_{water}$ refer to the $\delta^{18}O$ values of travertines and spring waters, respectively.

In this study, the average $\delta^{18}O_{water}$ value of active hot springs at Xiagei ($\delta^{18}O_{water}$ = −15.2‰ V-SMOW, Table 1) was used in the paleotemperature calculation.

The calculated results (Table 2, Figure 5) show that banded travertines, bedded travertines, recently formed travertines from Xiagei exhibit T_{cal} from 56.6 to 86.8 °C, from 53.0 to 62.9 °C, and from 44.3 to 62.0 °C, respectively. This indicates that the studied travertines were formed in moderate- to high-temperature hot spring environments. Water

temperatures of active hot springs at Xiagei vary from 32.0 to 63.1 °C (Table 1). However, according to our field observations, hot springs with high volumetric flow rates at Xiagei (e.g., S2; Table 1) often have vent temperatures of near 60.0 °C, slightly higher than T_{cal} of the recently formed travertines and close to T_{cal} of the bedded travertines (Table 2, Figure 5). This reflects that there were no significant vent temperature changes after the deposition of the studied bedded travertines.

The calculated paleotemperatures of the studied banded travertines generally range from 68 °C to 85 °C, higher than the vent temperatures of main active hot springs at Xiagei (ca. 60 °C; Table 2, Figure 5). This may indicate an unneglectable water temperature decrease between the places forming banded travertines and spring vents (i.e., vent temperature was lower than water temperature in the conduit). However, it must be noted that the vent temperatures in this study were measured in the margin areas of meter-scale vent pools. Thus, our measured temperatures might be slightly lower than the temperatures of spring waters outflowing from orifices just now, because the pool waters may have experienced important heat exchange with cool air (i.e., cooling). Such sample location-related temperature difference is common and unavoidable, especially for the large vent pools. Peng and Jones [44], for example, found that the spring water in the marginal areas of Eryuan pool (China) is 20 °C lower than the spring water near the Eryuan pool central vent. Therefore, simply extrapolating that there was a significant temperature decline between the places forming banded travertines and spring vents at Xiagei is still questionable. However, it is clear that fluid temperature changed a lot during the formation of the studied banded travertines, as shown by their great T_{cal} variation (56.6 °C to 86.8 °C).

5.2. Parent CO_2 Origin of Travertines

Parent CO_2 origins of spring-related carbonate deposits decide whether the deposits are tufas (also named meteogene travertines) or travertines (also called thermogene travertines) [45–47]. In this study, the equation (Equation (3)) from Chacko et al. [40] and the evaluated paleotemperatures (T_{cal}) were utilized to calculate the stable carbon isotope composition of parent CO_2 of the Xiagei Travertines ($\delta^{13}C_{parent\ CO_2}$).

$$1000\ \ln\alpha_{(parent\ CO_2\text{-}travertine)} = -0.10028 + 5.4173x - 2.5076x^2 + 0.47193x^3 - 0.0027046x^5 - 0.000059409x^6 \quad (3)$$

where $x = 10^6/T_{cal}^2$ and $\alpha_{(parent\ CO_2\text{-}travertine)}$ is:

$$\alpha_{(parent\ CO_2\text{-}CaCO_3)} = (\delta^{13}C_{parent\ CO_2} + 1)/(\delta^{13}C_{travertine} + 1) \quad (4)$$

The calculated results were listed in Table 2 and illustrated in Figures 5D and 6. Banded travertines at Xiagei have $\delta^{13}C_{parent\ CO_2}$ from −3.65‰ to −1.77‰ V-PDB (average = −2.44‰ V-PDB). In more detail, thick-laminated palisade banded travertines from Xiagei show $\delta^{13}C_{parent\ CO_2}$ between −2.93‰ to −1.77‰ V-PDB (average = −2.16‰ V-PDB), whereas thin-laminated composite banded travertines from Xiagei show a wider $\delta^{13}C_{parent\ CO_2}$ range (−3.65‰ to −1.88‰ V-PDB, average = −2.57‰ V-PDB). $\delta^{13}C_{parent\ CO_2}$ of bedded travertines from Xiagei falls into the banded travertine range and varies from −2.69‰ to −2.16‰ V-PDB (average = −2.45‰ V-PDB). In contrast, $\delta^{13}C_{parent\ CO_2}$ of recently formed travertines at Xiagei is very different from $\delta^{13}C_{parent\ CO_2}$ of the Xiagei banded travertines and bedded travertines and is between −1.80‰ and −1.24‰ V-PDB (average = −1.43‰ V-PDB).

Parent CO_2 sources of travertines are complex, but they mainly include magmatic CO_2, soil-derived CO_2, and CO_2 related to (marine) carbonate decarbonation [45]. It is reported that soil-derived CO_2 has $\delta^{13}C_{CO_2}$ values lower than −10‰ V-PDB (C3 plant soils = −30‰ to −16‰ V-PDB, C4 plant soils = −18‰ to −10‰ V-PDB; [48,49]. Magmatic CO_2 has $\delta^{13}C$ values from −7‰ to −5‰ V-PDB [50], while CO_2 related to (marine) carbonates decarbonation often has more positive $\delta^{13}C$ values (>1‰ V-PDB) [43,51]. The calculated $\delta^{13}C_{parent\ CO_2}$ ranges of the Xiagei fossil banded travertines, bedded travertines, and re-

cently formed travertines are all between the (marine) carbonate-related CO_2 zone and the magmatic CO_2 zone (Figure 6), instead of falling into any of the three typical CO_2 source areas. This largely suggests a possible mixing from (marine) carbonate decarbonation-related CO_2 and magmatic CO_2 and confirms that the Xiagei travertines are 'real' (thermogene) travertines, instead of tufas. Such inference (i.e., combined contribution of (marine) carbonate decarbonation-related CO_2 and magmatic CO_2) is consistent with early studies on hot spring gases at Xiagei and surrounding areas [52,53].

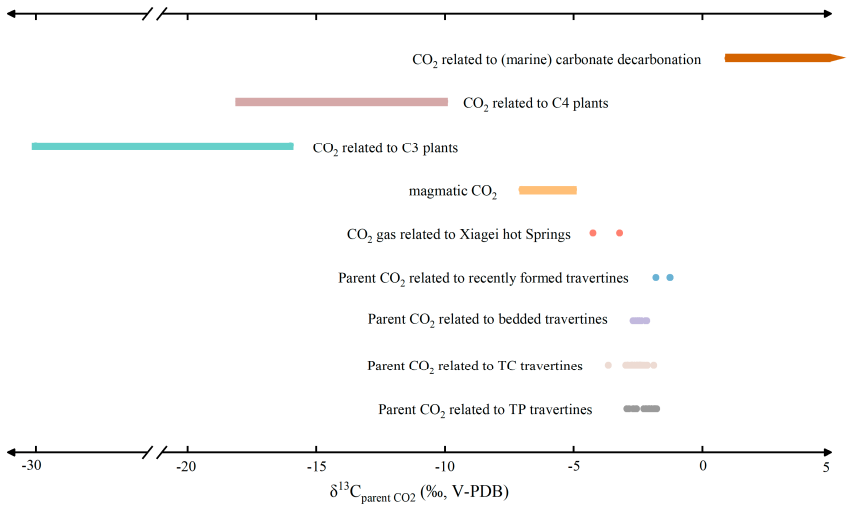


Figure 6. $\delta^{13}C_{parent\ CO_2}$ of the travertines from Xiagei, Shangri-La, China, according to the equation established by Chacko et al. [40]. In comparison with the $\delta^{13}C$ values from CO_2 gas related to Xiagei hot springs [53], magmatic CO_2 [50], CO_2 related to C3 and C4 plants [48,49], and marine carbonate decarbonation [43,51]. TP: thick-laminated crystalline crust; TC: thin-laminated composite crystalline crust.

Notably, the magmatism is lacking now in the Xiagei hydrothermal system (near the Jinshajiang fault zone) in the eastern Tibetan plateau. Thus, the detected magmatic source CO_2 for travertine samples might indicate a hypogene origin. As shown in Figure 1A, the Jinshajiang fault zone is important for the formation of Xiagei travertines as active large-scale strike-slipping, apart-pull basins and metamorphic core complexes are present [54,55], which provides ideal tectonic-environments for Paleogene mantle-derived high-K magmatism [54]. In addition, the Tibetan plateau has been a site for lithospheric delamination since about 40 Ma and is marked by intense and intensive intraplate, mantle-derived high-K magmatism [33,54]. Therefore, the magmatic-derived CO_2 for the Xiagei travertines probably indicates that the lithospheric mantle beneath the Jinshajiang fault zone is/was sinking, which led to the asthenosphere upwelling and subsurface accumulation of magmatic-derived CO_2 that was transported through the lithosphere via these large-scale faults.

Both (marine) carbonate decarbonation-related CO_2 and magmatic CO_2 are 'external' carbon sources. The Xiagei travertines were here also considered to receive some 'internal' carbon from marine carbonate rocks. As shown in Figure 1 and Table 1, marine carbonate rocks (mainly Late Paleozoic) are distributed in the study area and active hot springs have high Ca^{2+} concentrations (e.g., Springs S1 to S3 show Ca^{2+} concentrations from 120 to 151 mg/L) and low SO_4^{2-} concentrations (average = 50.5 mg/L). This largely reflects that marine carbonate dissolution also play a role in supplying carbon to the Xiagei travertines. Assuming that (1) HCO_3^- in spring waters at Xiagei was the mixing product of external carbon (i.e., magmatic CO_2 and carbonate decarbonation-related CO_2: $CO_2 + 2H_2O \rightarrow HCO_3^- + H^+$) and internal carbon (i.e., dissolution of Ca-carbonate rocks: $CaCO_3 + CO_2$

$\rightarrow 2HCO_3^- + Ca^{2+}$) and (2) Ca^{2+} in spring waters from Xiagei originated mainly from Ca-carbonate rock dissolution, the following equation can be obtained:

$$C_{total} = C_{external} + C_{internal} = C_{external} + C_{Ca} \quad (5)$$

where C_{total}, $C_{external}$, $C_{internal}$, and C_{Ca} represent the molar concentrations of HCO_3^-, external carbon, internal carbon, and Ca^{2+}, respectively.

Using the water data in Table 1, C_{total} and C_{Ca} in hot spring waters from Xiagei can be calculated. The calculated C_{total} and C_{Ca} are between 12.4 and 16.4 mM and between 0.90 and 3.78 mM, respectively, and the calculated C_{Ca}/C_{total} ratios vary from 10.2% to 24.2%, indicating the unneglectable role of Ca-carbonate dissolution in supplying carbon to the Xiagei travertines. However, it must be emphasized that the above calculations are not exact, because other processes (such as passive CO_2 degassing and carbonate precipitation) which are common in travertine systems [56–59] and can change HCO_3^- and Ca^{2+} concentrations in spring waters were not taken into consideration in our calculations.

5.3. Lithofacies of Banded Travertines Controlled by Water Temperature

There were two lithofacies of banded travertines at Xiagei: thick-laminated crystalline crust and thin-laminated composite crystalline crust. These two lithofacies display different features, especially in crystal sizes and morphologies. Calcite crystals in the thick-laminated crystalline crust are large and palisade-like, whereas calcite crystals in the thin-laminated composite crystalline crust are diverse but small in size. Recent studies have shown that the fluctuations of hydrodynamic conditions and hydrochemical composition of thermal fluids and microbial mediation can lead to the formation of calcite crystals of various sizes at thermal springs [28,60,61]. Jones and Renaut [62] and Jones [60] adopted a general term, 'driving force', to describe the growth condition of $CaCO_3$ precipitation in hot springs: the larger driving force, the more irregular $CaCO_3$ crystals. However, directly measuring 'driving force' is impossible for researchers, because it may be affected by many parameters, such as CO_2 degassing, water temperature, saturation index of $CaCO_3$, flow velocity, pH, and microbial effect [10,63–65]. These indicate that banded travertine precipitation is a complex process controlled by multiple factors/processes.

With respect to the two lithofacies of banded travertines at Xiagei, one possible factor controlling their crystal shapes and sizes might be water temperature. As shown in Table 2 and Figure 5D, the thick-laminated crystalline crust at Xiagei mainly displays T_{cal} over 80 °C, which is significantly higher than most of the T_{cal} values of the thin-laminated composite crust (generally below 72 °C). Theoretically, temperature increase would lower $CaCO_3$ and CO_2 solubility (when water temperature is below 155 °C) [66,67], promoting $CaCO_3$ precipitation. As a result, the thick-laminated crystalline crust was interpreted to be formed with a precipitation rate faster than the thin-laminated composite crystalline crust. Such inference agrees with the crystal size and morphology of these two lithofacies: rapid $CaCO_3$ precipitation formed large palisade crystals of the thick-laminated palisade crystalline crust, while relatively slow $CaCO_3$ precipitation generated small crystals of the thin-laminated composite crystalline crust.

However, some of the thick-laminated palisade crystalline crust samples (e.g., Samples 1, 2 and 3; Figures 4 and 5B,C; Table 2) show similar $\delta^{18}O$ and T_{cal} to the thin-laminated composite crystalline crust. Therefore, water temperature is an important but not decisive factor controlling the calcite crystal size and shape in the Xiagei banded travertines. Indeed, recently, Luo et al. [68] argued that $CaCO_3$ precipitation at the hypogean solid-water interface (i.e., banded travertine precipitation environments) was (at least) controlled by original fluid chemical composition, temperature, pressure, and fluid pathways. Thus, any change in fluid chemical composition (e.g., Ca^{2+} and HCO_3^- concentrations), CO_2 partial pressure in surrounding environments, and conduit morphology may significantly alter the precipitation rate of $CaCO_3$ at the hypogean solid–water interface. Unfortunately, these changes were difficult to evaluate only based on carbon and oxygen isotope compositions of banded travertines.

The thin-laminated composite crystalline crust is characterized by the appearance of diverse calcite crystals with different shapes and sizes (dendritic crystals, fan crystals, platy crystals, granular crystals, and micrite), whereas the thick-laminated palisade crystalline crust is compositionally simple. This may indicate a steady formation environment of the thick-laminated palisade crystalline crust and reflect that the formation condition of the thin-laminated composite crystalline crust underwent striking and rapid changes. Indeed, dendritic crystals, fan crystals, platy crystals, granular crystals, and micrite are often interpreted to be formed in different environments [38,60,69]. For example, fan crystals tend to be generated in turbulent water conditions [38,70–72], while platy crystals are often produced at near boiling conditions (>80 °C) [62,73,74].

5.4. Comparison with Banded Travertines from Other Areas

In Table 3 and Figure 7, the Xiagei banded travertines were compare with banded travertines (also sometimes named travertine veins) from other areas around the word [13,18,24,75,76] to examine their microscopic and stable carbon and oxygen isotopic differences. All banded travertines are found to be mainly composed of calcite and /or aragonite crystalline crusts (Table 3), but their microscopic features, such as crystal sizes and types are diverse, indicating the complex precipitation conditions/processes of banded travertines. For example, diverse calcite crystals have been described in the thin-laminated crystalline crust at Xiagei, probably representing changeable travertine formation environments. Note that elongated palisade calcite and/or aragonite crystals are commonly described in banded veins and are hardly seen in non-vein sediments of travertines. It may indicate that this texture can represent a typical lithofacies related to banded travertines. In addition, the banded travertines with diverse crystal morphologies, such as those from Semproniano (Italy), Kamara (Turkey), Gölemezli (Turkey), and Xiagei (China), are usually characterized by wide paleo-temperature ranges (Table 3). This might indicate that temperature plays an important role in controlling the microscopic features of banded travertines.

All the summarized banded travertines, excluding the Semproniano village giant veins [75], are characterized by good positive correlations between $\delta^{13}C$ and $\delta^{18}O$ values (Figure 7), probably indicating these banded travertines precipitated under non-equilibrium conditions (in more detail, fast CO_2 degassing). Using $\delta^{13}C$ values to gain the fluid CO_2 origins of spring related carbonate deposits is commonly used in earlier studies [13,18,39,75]. The parent CO_2 from all banded travertine was found to be largely derived from mixing sources (Table 3). However, the result shows that the $\delta^{13}C$ ranges of the banded travertine in different places are diverse. Especially, $\delta^{13}C$ of the Semproniano giant vein falls into a wider range, whereas $\delta^{13}C$ of travertines from Xiagei and other locations (Figure 7) exhibits relatively narrow isotopic variation. Berardi et al. [75] proposed that the long-lived giant vein underwent multiple tectonic events, spanning at least 650 and 85 ka. Thus, tectonic activities may play a non-negligible role in changing the $\delta^{13}C$ composition of the travertine vein. For instance, frequent tectonic activities may cause rapid $\delta^{13}C$ variations, while strong tectonic activities, like big earthquakes, may even modify thermal fluid circulation pathways and lead to significant $\delta^{13}C$ changes of banded travertines. According to Kele et al. [43], $\delta^{18}O$ values of travertines can be easily affected by fluid origins, evaporation rates and fluid temperature changes. In most travertine systems, the $\delta^{18}O$ values of travertines can be used to reflect the water temperature and $\delta^{18}O$ of the parent water. Taking into account the calculated paleo-temperatures, all the banded travertines in Table 3 are precipitated from moderate- to high-temperature hot springs, which further indicates that the fissure ridge is related to hot springs rather than cold springs. Overall, the comparison shows that $\delta^{13}C$ and $\delta^{18}O$ records in banded travertines might be useful for the assessment of tectonic activities and paleo-fluids.

Table 3. Comparison of banded veins from Xiagei and those from other places. Except Pamukkale and Reşadiye, the calculated temperature of other locations and Xaigei using the equation from Kele et al. [39]. Blank = no data.

Location	Classification	Characteristics	Lithofacies	Components	T (°C)	Fluid Origins
Semproniano Village, Italy [75]	Banded travertine	A giant structure characterized by a minimum thickness of 50 m	Crystalline crust	Complex, such as elongate V-like-shapes crystals, can reach to 2 cm.	34 ± 2 to 71 ± 7	Water is meteoric origin. CO_2 originated from limestone decarbonation with CO_2 of igneous origin
Semproniano Village, Italy [75]	Calcite vein	Veins cutting through carbonate rocks, reach to 5 cm thick			49 ± 4 to 56 ± 5	
I Vignacci, Italy [75]	Banded travertine	Composed of subvertical NW–SE-striking bands, located at an altitude of about 430 m a.s.l.			43 ± 3	Water is meteoric origin. CO_2 originated from limestone decarbonation with CO_2 of igneous origin
Kamara, Turkey [13]	Banded travertine	Bands up to 1 m thick		(a) The palisade/columnar structure made of bladed, rhombohedral/prismatic elongated crystals; (b) The botryoidal structure composed of fan-like splays of acicular/needle-like crystals, mm-to cm thick.	55 to 80	Water is meteoric origin. Parent CO_2 from magmatic, decarbonation of marine carbonate rocks and organic-sedimentary
Kamara, Turkey [13]	Calcite vein	These calcite veins isolate cm- to dm-thick volumes of hosting sediments.		Mm-thick, fibrous onyx-like calcite/aragonite crystals.	44 to 57	
Gölemezli, Turkey [18]	Banded travertine	Onyx-like, up to 12 m in width.		(a)Type A band, palisade/columnar, acicular/needle-like crystals, up to cm-long; (b) Type B band, micro-crystalline calcite, up to mm-thick.	53 to 76	Water is meteoric origin; Parent CO_2 from crustal- and mantle-derived CO_2.
Gölemezli, Turkey [18]	Calcite vein	Localized brecciation, formed in late deformational process, thickness ranges from 15 to 50 cm.		Few millimeter calcite crystals	60 to 65	
Pamukkale, Turkey [24,43]	Banded travertine	The band thickness varies from a few centimeters to 10 cm, mineral type: calcite and aragonite.		Radial, needle-shaped elongated crystals with length of about 0.5 to 1 mm	<60	Water is meteoric origin; Parent CO_2 from crustal- and mantle-derived CO_2.
Reşadiye, Turkey [24,77]	Banded travertine	Except typical bands, the travertines are detritus-free, porous, moderately crystalline, mineral type: calcite		Radial, needle-shaped elongated crystals with length of about 1 to 2 mm	<60	Water is meteoric origin; Parent CO_2 from crustal- and mantle-derived CO_2.
Ballık, Turkey [78]	Calcite vein	Cross-cutting the micritic travertine host rock, millimeter-thick to centimeter-thick		Micrite and fine-crystalline (<50 μm) calcite crystals, elongated coarse-crystalline sparite		
Utah, USA [76]	Carbonate vein	(a)Thin veins with characterized by isolated millimeter-thick calcium carbonate veins and 3D dense network veins; (b) Thick carbonate veins, up to 1 m thick; mineral type: calcite and aragonite.		Elongate V-like-shapes crystals, can reach to 1 mm.		
Xiagei, China this study	Banded travertine	Exposed in the center of fissure ridge, approximately 1.5 m.		Thick-laminated palisade crystalline crust: palisade crystals (from 1 to 3 cm long), thin-laminated composite crystalline crust: short-columnar crystals, dendritic crystals, platy crystals, fan crystals, granular crystals, and calcite micrite (less than 1 cm).	68 to 85	Water is meteoric origin; Parent CO_2 from (marine) carbonate decarbonation-related CO_2 and magmatic CO_2.

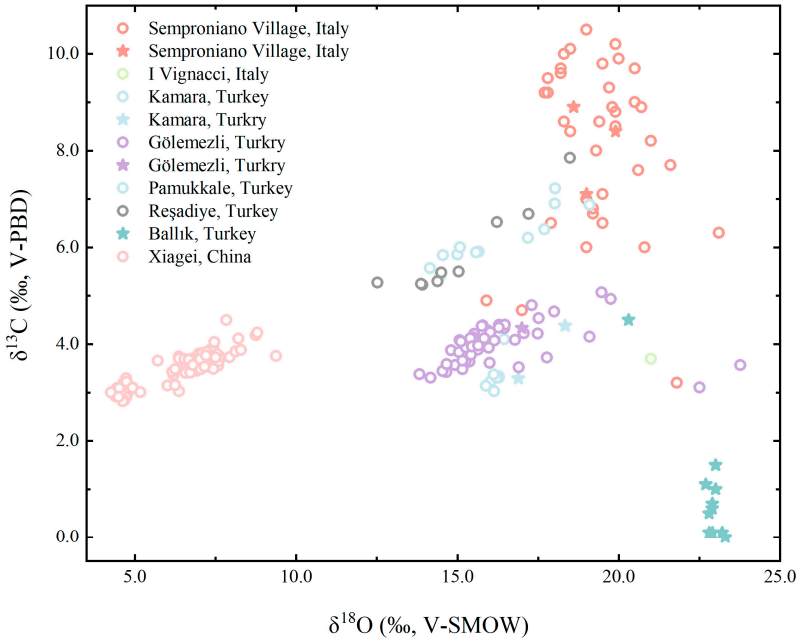


Figure 7. $\delta^{13}C$ and $\delta^{18}O$ values of banded calcite veins from Xiagei and those from other examples.

6. Conclusions

This study investigated the lithofacies and stable carbon and oxygen isotope geochemistry of banded travertines from fissure ridge-type travertine (Xiagei, China). Two lithofacies were recognized in the Xiagei banded travertines: thick-laminated palisade crystalline crust and thin-laminated composite crystalline crust. Parent CO_2 of the Xiagei banded travertines mainly originated from limestone decarbonation of marine carbonates, but they also received the contribution from magmatic CO_2. The magmatic-derived CO_2 may also demonstrate the sinking of the lithospheric mantle beneath the Jinshajiang fault zone. Additionally, dissolution of marine carbonate rock is considered to be important in providing carbon and calcium to the paleo-spring waters. Paleotemperatures precipitating the Xiagei banded travertines are from 56.6 °C to 86.8 °C, indicating moderate- to high-temperature spring environments. However, different lithofacies of banded travertines from Xiagei show distinct calculated paleotemperatures, suggesting temperature is a non-negligible control factor on the lithofacies of banded travertines. This study highlights the importance of depositional conditions (especially water temperature) on banded travertine lithofacies and reflects the significance of careful stable carbon and oxygen isotope analyses in the determination of paleo-fluid evaluation. The comparison between the banded travertines at Xiagei and other areas shows that microscopic features of banded travertines in different places is diverse, and banded travertines formed by calcite/aragonite with diverse morphologies are usually characterized by large paleo-temperature variations, further indicating that temperature plays a crucial role in controlling the microscopic characteristic of banded travertines. The comparison also implies that the stable carbon and oxygen isotopic characterization of banded travertines is likely an effective tool for assessing tectonic activities and paleo-fluids.

Author Contributions: Y.Y., L.L. (Lianchao Luo) and H.W. conceived this contribution. Y.Y., Z.L. and L.L. (Liang Li) conducted the field investigation. Y.Y., Z.L. and L.L. (Liang Li) performed the sample handling and data analysis. Y.Y. wrote the original draft of the paper. L.L. (Lianchao Luo) reviewed the original draft of the paper. All authors have read and agreed to the published version of the manuscript.

Funding: This research was financially supported by the National Natural Science Foundation of China (grant Nos. 41972116 and 41572097).

Data Availability Statement: The data that support the findings of this study are available in the text, figures and tables of this manuscript.

Acknowledgments: We are grateful to Lei Du for his help in field works. We also thank four anonymous reviewers for their detailed and constructive comments.

Conflicts of Interest: The authors declare no conflict of interest from their affiliation or funding.

References

1. Altunel, E.; Karabacak, V. Determination of horizontal extension from fissure-ridge travertines: A case study from the Denizli Basin, southwestern Turkey. *Geodin. Acta* **2005**, *18*, 333–342. [CrossRef]
2. Brogi, A.; Capezzuoli, E. Travertine deposition and faulting: The fault-related travertine fissure-ridge at Terme S. Giovanni, Rapolano Terme (Italy). *Int. J. Earth Sci.* **2008**, *98*, 931–947. [CrossRef]
3. Brogi, A.; Capezzuoli, E.; Alçiçek, M.C.; Gandin, A. Evolution of a fault-controlled fissure-ridge type travertine deposit in the western Anatolia extensional province: The Çukurbağ fissure-ridge (Pamukkale, Turkey). *J. Geol. Soc.* **2014**, *171*, 425–441. [CrossRef]
4. Brogi, A.; Capezzuoli, E.; Karabacak, V.; Alcicek, M.C.; Luo, L. Fissure ridges: A reappraisal of faulting and travertine deposition (travitonics). *Geosciences* **2021**, *11*, 278. [CrossRef]
5. De Filippis, L.; Anzalone, E.; Billi, A.; Faccenna, C.; Poncia, P.P.; Sella, P. The origin and growth of a recently-active fissure ridge travertine over a seismic fault, Tivoli, Italy. *Geomorphology* **2013**, *195*, 13–26. [CrossRef]
6. De Filippis, L.; Faccenna, C.; Billi, A.; Anzalone, E.; Brilli, M.; Soligo, M.; Tuccimei, P. Plateau versus fissure ridge travertines from Quaternary geothermal springs of Italy and Turkey: Interactions and feedbacks between fluid discharge, paleoclimate, and tectonics. *Earth-Sci. Rev.* **2013**, *123*, 35–52. [CrossRef]
7. Guo, L.; Riding, R. Rapid facies changes in Holocene fissure ridge hot spring travertines, Rapolano Terme, Italy. *Sedimentology* **1999**, *46*, 1145–1158. [CrossRef]
8. Karabacak, V.; Uysal, I.T.; Ünal-İmer, E.; Mutlu, H.; Zhao, J. U-Th age evidence from carbonate veins for episodic crustal deformation of Central Anatolian Volcanic Province. *Quat. Sci. Rev.* **2017**, *177*, 158–172. [CrossRef]
9. Mancini, A.; Capezzuoli, E.; Erthal, M.; Swennen, R. Hierarchical approach to define travertine depositional systems: 3D conceptual morphological model and possible applications. *Mar. Pet. Geol.* **2019**, *103*, 549–563. [CrossRef]
10. Della Porta, G. Carbonate build-ups in lacustrine, hydrothermal and fluvial settings: Comparing depositional geometry, fabric types and geochemical signature. In: Bosence, D.W.J., Gibbons, K.A., Le Heron, D.P., Morgan, W.A., Pritchard, T., Vining, B.A. Microbial Carbonates in Space and Time: Implications for Global Exploration and Production. *Geol. Soc. Lond. Spec. Publ.* **2015**, *418*, 17–68.
11. Altunel, E.; Hancock, P.L. Structural attributes of travertine-filled extensional fissures in the Pamukkale Plateau, Western Turkey. *Int. Geol. Rev.* **1996**, *38*, 768–777. [CrossRef]
12. Brogi, A.; Alçiçek, M.C.; Liotta, D.; Capezzuoli, E.; Zucchi, M.; Matera, P.F. Step-over fault zones controlling geothermal fluid-flow and travertine formation (Denizli Basin, Turkey). *Geothermics* **2021**, *89*, 101941. [CrossRef]
13. Brogi, A.; Alçiçek, M.C.; Yalçıner, C.Ç.; Capezzuoli, E.; Liotta, D.; Meccheri, M.; Rimondi, V.; Ruggieri, G.; Gandin, A.; Boschi, C.; et al. Hydrothermal fluids circulation and travertine deposition in an active tectonic setting: Insights from the Kamara geothermal area (western Anatolia, Turkey). *Tectonophysics* **2016**, *680*, 211–232. [CrossRef]
14. Brogi, A.; Capezzuoli, E. Earthquake impact on fissure-ridge type travertine deposition. *Geol. Mag.* **2014**, *151*, 1135–1143. [CrossRef]
15. De Filippis, L.; Billi, A. Morphotectonics of fissure ridge travertines from geothermal areas of Mammoth Hot Springs (Wyoming) and Bridgeport (California). *Tectonophysics* **2012**, *548–549*, 34–48. [CrossRef]
16. De Filippis, L.; Faccenna, C.; Billi, A.; Anzalone, E.; Brilli, M.; Ozkul, M.; Soligo, M.; Tuccimei, P.; Villa, I.M. Growth of fissure ridge travertines from geothermal springs of Denizli Basin, western Turkey. *Geol. Soc. Am. Bull.* **2012**, *124*, 1629–1645. [CrossRef]
17. Zhang, K.-J.; Li, Q.-H.; Yan, L.-L.; Zeng, L.; Lu, L.; Zhang, Y.-X.; Hui, J.; Jin, X.; Tang, X.-C. Geochemistry of limestones deposited in various plate tectonic settings. *Earth-Sci. Rev.* **2017**, *167*, 27–46. [CrossRef]
18. Capezzuoli, E.; Ruggieri, G.; Rimondi, V.; Brogi, A.; Liotta, D.; Alçiçek, M.C.; Alçiçek, H.; Bülbül, A.; Gandin, A.; Meccheri, M.; et al. Calcite veining and feeding conduits in a hydrothermal system: Insights from a natural section across the Pleistocene Gölemezli travertine depositional system (western Anatolia, Turkey). *Sediment. Geol.* **2018**, *364*, 180–203. [CrossRef]
19. Hancock, P.L.; Chalmers, R.M.L.; Altunel, E.; Çakir, Z. Travitonics: Using travertines in active fault studies. *J. Struct. Geol.* **1999**, *21*, 903–916. [CrossRef]
20. Sağlam Selçuk, A.; Erturaç, M.K.; Üner, S.; Özsayın, E.; Pons-Branchu, E. Evolution of Çamlık fissure-ridge travertines in the Başkale basin (Van, Eastern Anatolia). *Geodin. Acta* **2016**, *29*, 1–19. [CrossRef]
21. Haluk Selim, H.; Yanik, G. Development of the Cambazlı (Turgutlu/MANISA) fissure-ridge-type travertine and relationship with active tectonics, Gediz Graben, Turkey. *Quat. Int.* **2009**, *199*, 157–163. [CrossRef]
22. Curewitz, D.; Karson, J.A. Structural settings of hydrothermal outflow: Fracture permeability maintained by fault propagation and interaction. *J. Volcanol. Geotherm. Res.* **1997**, *79*, 149–168. [CrossRef]

23. Matera, P.F.; Ventruti, G.; Zucchi, M.; Brogi, A.; Capezzuoli, E.; Liotta, D.; Yu, T.-L.; Shen, C.-C.; Huntington, K.W.; Rinyu, L.; et al. Geothermal fluid variation recorded by banded Ca-carbonate veins in a fault-related, fissure ridge-type travertine depositional system (Iano, southern Tuscany, Italy). *Geofluids* **2021**, *2021*, 1–28. [CrossRef]
24. Rizzo, A.L.; Uysal, I.T.; Mutlu, H.; Ünal-İmer, E.; Dirik, K.; Yüce, G.; Caracausi, A.; Italiano, F.; Misseri, M.; Temel, A.; et al. Geochemistry of Fluid Inclusions in Travertines From Western and Northern Turkey: Inferences on the Role of Active Faults in Fluids Circulation. *Geochem. Geophys. Geosyst.* **2019**, *20*, 5473–5498. [CrossRef]
25. Uysal, I.; Feng, Y.; Zhao, J.; Altunel, E.; Weatherley, D.; Karabacak, V.; Cengiz, O.; Golding, S.; Lawrence, M.; Collerson, K. U-series dating and geochemical tracing of late Quaternary travertine in co-seismic fissures. *Earth Planet. Sci. Lett.* **2007**, *257*, 450–462. [CrossRef]
26. Uysal, I.T.; Feng, Y.-x.; Zhao, J.-x.; Isik, V.; Nuriel, P.; Golding, S.D. Hydrothermal CO_2 degassing in seismically active zones during the late Quaternary. *Chem. Geol.* **2009**, *265*, 442–454. [CrossRef]
27. Chen, Q. Studies on Geochemistry of the Permian Basalts in Shangri-La County YunNan Province China. Master's Thesis, University of Geosciences, Beijing, China, 2017.
28. Jones, B.; Peng, X. Intrinsic versus extrinsic controls on the development of calcite dendrite bushes, Shuzhishi Spring, Rehai geothermal area, Tengchong, Yunnan Province, China. *Sediment. Geol.* **2012**, *249–250*, 45–62. [CrossRef]
29. Li, L.; Wang, Y. Application of geophysical method to geothermal resource prospecting in Xianggelila Basin, Yunnan. *Carsologica Sin.* **2004**, *23*, 187–195.
30. Wang, Y. *Research Report on Geothermal Resources Exploration in Shangri La Basin, Diqing Tibetan Autonomous Prefecture, Yunnan Province*; Yunnan Exploration Development Bureauof Geology Mineral Resources: Yunnan, China, 2003.
31. Wang, Y.; Yang, S.Y. The geothermal feature and exploring prospect of the Xianggelila Basin in Narthwestern Yunnnan, China. *Bull. Mineral. Petrol. Geochem.* **2003**, *33*, 265–269, 272.
32. Zheng, Y.H. *Characteristics of the Tianshengqiao and Xiagei Hots Prings in Shangrila County of Yunnan and Analysis of the Formation of the Travertine*; China University of Geosciences: Beijing, China, 2015.
33. Zhang, K.-J.; Zhang, Y.-X.; Tang, X.-C.; Xia, B. Late Mesozoic tectonic evolution and growth of the Tibetan plateau prior to the Indo-Asian collision. *Earth-Sci. Rev.* **2012**, *114*, 236–249. [CrossRef]
34. Zhang, K.-J.; Zhang, Y.-X.; Li, B.; Zhong, L.-F. Nd isotopes of siliciclastic rocks from Tibet, western China: Constraints on provenance and pre-Cenozoic tectonic evolution. *Earth Planet. Sci. Lett.* **2007**, *256*, 604–616. [CrossRef]
35. Zhang, K.-J.; Xia, B.; Liang, X. Mesozoic–Paleogene sedimentary facies and paleogeography of Tibet, western China: Tectonic implications. *Geol. J.* **2002**, *37*, 217–246. [CrossRef]
36. Jackson, M.L. *Soil Chemical Analysis*; Prentice Hall: Englewood Cliffs, NJ, USA, 1958.
37. Parkhurst, D.L.; Appelo, C.A.J. Description of input and examples for PHREEQC version 3—A computer program for speciation, batch-reaction, one-dimensional transport, and inverse geochemical calculations. *US Geol. Surv. Tech. Methods* **2013**, *6*, 497.
38. Gandin, A.; Capezzuoli, E. Travertine: Distinctive depositional fabrics of carbonates from thermal spring systems. *Sedimentology* **2014**, *61*, 264–290. [CrossRef]
39. Kele, S.; Breitenbach, S.F.M.; Capezzuoli, E.; Meckler, A.N.; Ziegler, M.; Millan, I.M.; Kluge, T.; Deák, J.; Hanselmann, K.; John, C.M.; et al. Temperature dependence of oxygen- and clumped isotope fractionation in carbonates: A study of travertines and tufas in the 6–95 °C temperature range. *Geochim. Et Cosmochim. Acta* **2015**, *168*, 172–192. [CrossRef]
40. Chacko, T.; Cole, D.R.; Horita, J. Equilibrium Oxygen, Hydrogen and Carbon Isotope Fractionation Factors Applicable to Geologic Systems. *Rev. Mineral. Geochem.* **2001**, *43*, 1–81. [CrossRef]
41. Chafetz, H.S.; Guidry, S.A. Deposition and diagenesis of Mammoth Hot Springs travertine, Yellowstone National Park, Wyoming, U.S.A. *Can. J. Earth Sci.* **2003**, *40*, 1515–1529. [CrossRef]
42. Karabacak, V.; Uysal, I.T.; Mutlu, H.; Ünal-İmer, E.; Dirik, R.K.; Feng, Y.x.; Akıska, S.; Aydoğdu, İ.; Zhao, J.x. Are U-Th dates correlated with historical records of earthquakes? Constraints from coseismic carbonate veins within the North Anatolian Fault Zone. *Tectonics* **2019**, *38*, 2431–2448. [CrossRef]
43. Kele, S.; Özkul, M.; Fórizs, I.; Gökgöz, A.; Baykara, M.O.; Alçiçek, M.C.; Németh, T. Stable isotope geochemical study of Pamukkale travertines: New evidences of low-temperature non-equilibrium calcite-water fractionation. *Sediment. Geol.* **2011**, *238*, 191–212. [CrossRef]
44. Peng, X.; Jones, B. Patterns of biomediated $CaCO_3$ crystal bushes in hot spring deposits. *Sediment. Geol.* **2013**, *294*, 105–117. [CrossRef]
45. Pentecost, A. *Travertine*; Springer: Berlin/Heidelberg, Germany, 2005.
46. Pentecost, A.; Viles, H. A Review and Reassessment of Travertine Classification. *Géographie Phys. Et Quat.* **1994**, *48*, 305–314. [CrossRef]
47. Teboul, P.A.; Durlet, C.; Gaucher, E.C.; Virgone, A.; Girard, J.P.; Curie, J.; Lopez, B.; Camoin, G.F. Origins of elements building travertine and tufa: New perspectives provided by isotopic and geochemical tracers. *Sediment. Geol.* **2016**, *334*, 97–114. [CrossRef]
48. Claes, H.; Soete, J.; Van Noten, K.; El Desouky, H.; Marques Erthal, M.; Vanhaecke, F.; Özkul, M.; Swennen, R.; Reijmer, J. Sedimentology, three-dimensional geobody reconstruction and carbon dioxide origin of Pleistocene travertine deposits in the Ballık area (south-west Turkey). *Sedimentology* **2015**, *62*, 1408–1445. [CrossRef]
49. Vogel, J.C. Variability of Carbon Isotope Fractionation during Photosynthesis. In *Stable Isotopes and Plant Carbon-Water Relations*; Ehleringer, J.R., Hall, A.E., Farquhar, G.D., Eds.; Academic Press: San Diego, CA, USA, 1993; pp. 29–46.

50. Hoefs, J. *Stable Isotope Geochemistry*; Springer: Berlin/Heidelberg, Germany, 2009; Volume 201.
51. Rollinson, H. *Using Geochemical Data*; Cambridge University Press: Cambridge, UK, 1993; Volume 1.
52. Liu, Z.; Yuan, D. Features of geochemical variations in typical epikarst systems of China and thier environment significance. *Geol. Rev.* **2000**, *46*, 324–327.
53. Sheng, L.C. The Study of Deep Source CO_2 Degasification and Carbon Cycle in the Southwest of China. Ph.D. Thesis, Southwest University (China), Chongqing, China, 2007.
54. Xu, Y.; Zhu, J.; Hu, R.; Bi, X.; Yu, H.; Xu, L.; Liu, B.; Huang, M.; Sheng, X. Heterogeneous lithospheric mantle beneath the southeastern Tibetan Plateau: Evidence from Cenozoic high-Mg potassic volcanic rocks in the Jinshajiang–Ailaoshan Cenozoic magmatic belt. *J. Asian Earth Sci.* **2019**, *180*, 103849. [CrossRef]
55. Tapponnier, P.; Lacassin, R.; Leloup, P.H.; Schärer, U.; Dalai, Z.; Haiwei, W.; Xiaohan, L.; Shaocheng, J.; Lianshang, Z.; Jiayou, Z. The Ailao Shan/Red River metamorphic belt: Tertiary left-lateral shear between Indochina and South China. *Nature* **1990**, *343*, 431–437. [CrossRef]
56. Mancini, A.; Frondini, F.; Capezzuoli, E.; Galvez Mejia, E.; Lezzi, G.; Matarazzi, D.; Brogi, A.; Swennen, R. Porosity, bulk density and $CaCO_3$ content of travertines. A new dataset from Rapolano, Canino and Tivoli travertines (Italy). *Data Brief* **2019**, *25*, 104158. [CrossRef]
57. Mancini, A.; Frondini, F.; Capezzuoli, E.; Mejia, E.G.; Lezzi, G.; Matarazzi, D.; Brogi, A.; Swennen, R. Evaluating the geogenic CO_2 flux from geothermal areas by analysing quaternary travertine masses. New data from western central Italy and review of previous CO_2 flux data. *Quat. Sci. Rev.* **2019**, *215*, 132–143. [CrossRef]
58. Mancini, A.; Capezzuoli, E.; Brogi, A.; Swennen, R.; Ricci, L.; Frondini, F. Geogenie CO_2 flux calculations from the Late Pleistocene Tivoli travertines (Acque Albule Basin, Tivoli, Central Italy). *Ital. J. Geosci.* **2020**, *139*, 374–382. [CrossRef]
59. Uysal, I.T.; Ünal-İmer, E.; Shulmeister, J.; Zhao, J.-X.; Karabacak, V.; Feng, Y.-X.; Bolhar, R. Linking CO_2 degassing in active fault zones to long-term changes in water balance and surface water circulation, an example from SW Turkey. *Quat. Sci. Rev.* **2019**, *214*, 164–177. [CrossRef]
60. Jones, B. Review of aragonite and calcite crystal morphogenesis in thermal spring systems. *Sediment. Geol.* **2017**, *354*, 9–23. [CrossRef]
61. Mors, R.A.; Gomez, F.J.; Astini, R.A.; Mlewski, E.C.; Gérard, E. Physico-chemical and biological controls in a travertine system in the high Andes of northwestern Argentina. *Sediment. Geol.* **2022**, *439*, 106214. [CrossRef]
62. Jones, B.; Renaut, R.W. Origin of platy calcite crystals in hot-spring deposits in the Kenya Rift valley. *J. Sediment. Res.* **1995**, *68*, 913–927. [CrossRef]
63. Minissale, A.; Kerrick, D.M.; Magro, G.; Murrell, M.T.; Paladini, M.; Rihs, S.; Sturchio, N.C.; Tassi, F.; Vaselli, O. Geochemistry of Quaternary travertines in the region north of Rome (Italy): Structural, hydrologic and paleoclimatic implications. *Earth Planet. Sci. Lett.* **2002**, *203*, 709–728. [CrossRef]
64. Minissale, A. Origin, transport and discharge of CO_2 in central Italy. *Earth-Sci. Rev.* **2004**, *66*, 89–141. [CrossRef]
65. Della Porta, G.; Croci, A.; Marini, M.; Kele, S. Depositional architecture, facies character and geochemical signature of the Tivoli travertines (Pleistocene, Acque Albule Basin, Central Italy). *Riv. Ital. Di Paleontol. E Stratigr.* **2017**, *123*, 487–540.
66. Duan, Z.; Sun, R. An improved model calculating CO_2 solubility in pure water and aqueous NaCl solutions from 273 to 533 K and from 0 to 2000 bar. *Chem. Geol.* **2003**, *193*, 257–271. [CrossRef]
67. Spycher, N.; Pruess, K. A Phase-Partitioning Model for CO_2–Brine Mixtures at Elevated Temperatures and Pressures: Application to CO_2-Enhanced Geothermal Systems. *Transp. Porous Media* **2010**, *82*, 173–196. [CrossRef]
68. Luo, L.; Capezzuoli, E.; Rogerson, M.; Vaselli, O.; Wen, H.; Lu, Z. Precipitation of carbonate minerals in travertine-depositing hot springs: Driving forces, microenvironments, and mechanisms. *Sediment. Geol.* **2022**, *438*, 106207. [CrossRef]
69. Luo, L.; Wen, H.; Li, Y.; You, Y.; Luo, X. Mineralogical, crystal morphological, and isotopic characteristics of smooth slope travertine deposits at Reshuitang, Tengchong, China. *Sediment. Geol.* **2019**, *381*, 29–45. [CrossRef]
70. Guo, L.I.; Riding, R. Aragonite laminae in hot water travertine crusts, Rapolano Terme, Italy. *Sedimentology* **1992**, *39*, 1067–1079. [CrossRef]
71. Liu, Z.; Li, H.; You, C.; Wan, N.; Sun, H. Thickness and stable isotopic characteristics of modern seasonal climate-controlled sub-annual travertine laminas in a travertine-depositing stream at Baishuitai, SW China: Implications for paleoclimate reconstruction. *Environ. Geol.* **2006**, *51*, 257–265. [CrossRef]
72. Okumura, T.; Takashima, C.; Shiraishi, F.; Kano, A. Textural transition in an aragonite travertine formed under various flow conditions at Pancuran Pitu, Central Java, Indonesia. *Sediment. Geol.* **2012**, *265–266*, 195–209. [CrossRef]
73. Simmons, S.F.; Arehart, G.; Simpson, M.P.; Mauk, J.L. Origin of massive calcite veins in the Golden Cross low-sulfidation, epithermal Au-Ag deposit, New Zealand. *Econ. Geol.* **2000**, *95*, 99–112. [CrossRef]
74. Simmons, S.F.; Browne, P.R.L. Hydrothermal minerals and precious metals in the Broadlands-Ohaaki geothermal system: Implications for understanding low-sulfidation epithermal environments. *Econ. Geol.* **2000**, *95*, 971–999. [CrossRef]
75. Berardi, G.; Vignaroli, G.; Billi, A.; Rossetti, F.; Soligo, M.; Kele, S.; Baykara, M.O.; Bernasconi, S.M.; Castorina, F.; Tecce, F.; et al. Growth of a Pleistocene giant carbonate vein and nearby thermogene travertine deposits at Semproniano, southern Tuscany, Italy: Estimate of CO_2 leakage. *Tectonophysics* **2016**, *690*, 219–239. [CrossRef]

76. Frery, E.; Gratier, J.-P.; Ellouz-Zimmerman, N.; Loiselet, C.; Braun, J.; Deschamps, P.; Blamart, D.; Hamelin, B.; Swennen, R. Evolution of fault permeability during episodic fluid circulation: Evidence for the effects of fluid–rock interactions from travertine studies (Utah–USA). *Tectonophysics* **2015**, *651–652*, 121–137. [CrossRef]
77. Süer, S.; Güleç, N.; Mutlu, H.; Hilton, D.R.; Çifter, C.; Sayin, M. Geochemical Monitoring of Geothermal Waters (2002–2004) along the North Anatolian Fault Zone, Turkey: Spatial and Temporal Variations and Relationship to Seismic Activity. *Pure Appl. Geophys.* **2008**, *165*, 17–43. [CrossRef]
78. Desouky, H.E.; Soete, J.; Claes, H.; Özkul, M.; Vanhaecke, F.; Swennen, R.; Ariztegui, D. Novel applications of fluid inclusions and isotope geochemistry in unravelling the genesis of fossil travertine systems. *Sedimentology* **2015**, *62*, 27–56. [CrossRef]

Disclaimer/Publisher's Note: The statements, opinions and data contained in all publications are solely those of the individual author(s) and contributor(s) and not of MDPI and/or the editor(s). MDPI and/or the editor(s) disclaim responsibility for any injury to people or property resulting from any ideas, methods, instructions or products referred to in the content.